High Flux Helium Irradiation of Dispersion-Strengthened Tungsten Alloys and Effects of Heavy Metal Impurity Layer Deposition

E. Lang[*1], A. Kapat[1], T.W. Morgan[2], J.P. Allain[3]

[1]*Department of Nuclear, Plasma, and Radiological Engineering, University of Illinois at Urbana-Champaign, Urbana, IL, USA*
[2]*DIFFER - Dutch Institute for Fundamental Energy Research, De Zaale 20, 5612 AJ Eindhoven, the Netherlands*
[3]*Ken and Mary Alice Lindquist Department of Nuclear Engineering, Pennsylvania State University, State College, PA, USA*

Abstract

Tungsten has been chosen as the plasma-facing material (PFM) for the divertor region in ITER and also a candidate PFM for future plasma-burning nuclear fusion reactors. During fusion device operation, PFMs will be exposed to low-energy He irradiation at high temperatures, resulting in sub-surface bubbles and surface morphology changes such as pores and fuzz. Carbide dispersion-strengthened W materials may enhance the ductility of W, but their behavior under high flux He irradiation remains unclear. In this work, the response of dispersion-strengthened tungsten materials to high flux, low energy He irradiation at high temperature is examined. Tungsten alloyed with 1, 5, or 10 wt. % tantalum carbide or titanium carbide exposed to these conditions result in surface pores, coral-like feature growth and sub-surface helium bubbles. Reactor-relevant helium irradiation ($5x10^{26}$ m^{-2} fluence) combined with high powered laser pulses to simulate off-normal reactor events does not significantly alter the surface morphology, as the surface nanostructures appear stable and cracks are only observed on a localized region of one sample. However, specimens show the development of an impurity layer on the surface, likely impurity deposition from the sample holder during irradiation, resulting in a mixed material layer on the surface. Helium bubbles exist in this impurity layer, and obscure conclusions about helium interactions with the carbide dispersoids. Nonetheless, it is clear that the dispersoid microstructure limits He bubble formation and subsequent surface nanostructuring, attributed to the dispersoid composition.

Keywords: Dispersion-strengthened tungsten; Tungsten; Helium irradiation; Surface impurity layer

Highlights: Exposure of TaC and TiC-doped W to low energy He ions resulted in surface pores and coral-like morphological growth; During irradiation, a Mo-rich impurity layer is deposited on the specimen

surfaces; Helium bubbles are observed in the sub-surface and in the impurity layer, resulting in a mixed material surface that may be a surrogate for those that are observed in a fusion reactor.

*Corresponding Author Address: 104 S. Wright St., Urbana, IL 61801, USA

*Corresponding Author Email: ejlang2@illinois.edu

1. Introduction

The divertor region of nuclear fusion reactors presents a harsh environment, as materials chosen for this application must withstand high thermal loads, high particle fluxes of H and He, and high mechanical stresses induced by temperature gradients. The current plasma-facing material of choice is tungsten (W), as its high melting point, high sputtering threshold, and high thermal conductivity make it a good candidate material for the harsh fusion reactor environment [1, 2]. However, the mechanical drawbacks intrinsic in W limit its applications: W has a high ductile-brittle transition temperature and is embrittled under irradiation and recrystallization [3-5].

The divertor region will expose materials to high fluences of low energy He irradiation. Under high temperature He irradiation at incident ion energies from ~10 eV to 10's of keV's, W undergoes surface and sub-surface modifications. Most relevant for the divertor region specifically, low energy He ions below the knock-on damage threshold (~200 eV) can cause the formation of nanofeatures on high temperature W surfaces, ranging from pores to ripples to fiber-form fuzz as the He fluence is increased [6-16]. Incident He atoms settle at intrinsic lattice defects, such as vacancies and interstitials. At high temperature, He atoms migrate and form He-vacancy (He-V) clusters. These He-V clusters can trap numerous He atoms and can grow via loop punching or trap mutation and associate with tungsten vacancies (V) to form He bubbles [17]. Bubbles continue to grow due to migration and aggregation of smaller He bubbles, eventually forming large sub-surface gas-filled bubbles [17-19]. At high temperature, these bubbles migrate to the surface, likely causing the development of the surface pinhole structure [18]. At temperatures above 1000 K and fluences above 10^{25} m^{-2}, a fine, fiber-form structure develops as the surface further roughens [11]. The exact mechanisms governing the transition from sub-surface bubbles to formation of tendrils is not well

understood, multiple theories describing the growth of fuzz due to the presence of bubbles have been proposed indicating an important role of He bubbles on fuzz formation [20].

It is known that W grain boundaries act as sinks for defects including interstitial He atoms, vacancies, and He bubbles; indeed, ultra-fine grained W materials demonstrate greater resistance to He-induced morphology development [11, 12]. Thus, control of interfaces in the W matrix may alter He bubble distribution and at regions close to the surface, the resistance to surface tendril formation.

The thermomechanical issues with tungsten described above, namely its low ductility, have motivated the study of alternate W systems that have properties that are enhanced in the irradiation environment and can adapt to the harsh conditions. Recently, dispersion-strengthened tungsten (DS-W) materials have received interest as plasma-facing components. Dispersion-strengthened W alloys are tungsten-based materials strengthened with dispersed second phase particles, such as oxide-strengthened and carbide-strengthened materials [21-27]. The behavior of carbide-strengthened tungsten alloys has been preliminarily studied under He irradiation. Tungsten with titanium carbide has shown resistance to irradiation-induced hardening by high energy He ions [25-28], yet still is prone to nanostructure formation under low energy He bombardment [28, 29]. Various W grades with different second phases (TiC, ZrC, Y_2O_3, La_2O_3, Re) have also shown differing levels of He-induced surface modification, but none prevent the development of nanostructuring [28-30].

H-mode confinement in tokamaks will cause the development of edge localized modes (ELMs) that will deliver transient high heat and particle fluxes to the first wall and divertor. Studies of ELM-like transient heat loads on W materials have been performed with and without simultaneous He irradiation, causing the development of cracking, surface roughening, localized melting, and a reduction in the thickness of the He-induced surface morphology and alteration of the sub-surface bubble behavior [31-34].

In this paper, we report the results of high fluence, low energy He-irradiation-induced modifications of TiC and TaC, dispersion-strengthened W composite materials with and without synergistic plasma pulsing. The effects of the type and concentration of the added second phase dispersoids and the simultaneous high heat flux on the surface and sub-surface morphology material response will be presented.

Post- irradiation characterization of the surface composition, sub-surface bubble development, and surface morphology reveal an important link between the He-induced damage and the alloying elements of the W-based material.

2. Materials and Methods

The experimental work presented investigated two different types of dispersion-strengthened W materials: W doped with TaC or TiC. These alloys were fabricated with 1, 5, or 10 wt.% added carbide via spark plasma sintering. When referring to samples, the following naming convention is used: W-*x*TiC has *x* wt.% added TiC (x = {1,5,10}), while W-*y*TaC has *y* wt.% added TaC (y = {1,10}). More details on the fabrication, microstructure, and composition of these materials can be found elsewhere [35]. Samples were cut into 10mm diameter, 2mm thick half-discs, and mechanically polished to a mirror-like finish using 0.05 μm diamond suspension prior to irradiation. Two specimens were exposed simultaneously, placed side-by-side in the sample holder.

The He^+ irradiations were performed at Magnum-PSI at the Dutch Institute for Fundamental Energy Research (DIFFER) [36-38]. Two sets of samples were exposed to pure He plasmas: one set with and one set without simultaneous high heat flux (HHF) pulsing. A high-powered Nd:YAG laser was used to expose samples to pulsed temperature excursions during He plasma exposure. In these experiments, the pulse duration was ~1 ms and pulse frequency 0.1 Hz. A bias of -33V was applied to the target and with electron temperatures ~1.5-2 eV, setting the incident ion energy to ~30 eV. The temperature was monitored by a FLIR fast IR camera (SC 7500-MB) and a Far Associates multiwavelength pyrometer (FMPI-I).

A multi-sample holder that allowed for simultaneous exposure of multiple samples was utilized for the plasma exposures. One set of samples was exposed to pure He plasma without laser pulsing. The ion flux during these exposures and target temperatures were varied slightly to optimize source operation: the fluxes were $3.5\text{x}10^{23}$-$3\text{x}10^{24}$ $\text{m}^{-2}\text{s}^{-1}$ and temperatures 900-1100 C. The total fluence of exposed samples was $5\text{x}10^{26}$ m^{-2}. A second set of samples were exposed to the same irradiation conditions, but with simultaneous laser pulses. The transient heat load density was ~0.1-0.5 GW m^{-2}, resulting in a temperature excursion of

~250 C on top of the base temperatures of ~900-1100 C. **Table 1** summarizes the irradiation parameters on specified samples.

Surface morphology was investigated with scanning electron microscopy (SEM) using a JEOL 7000F Analytical SEM, an FEI Helios 600i Dual Beam FIB/SEM, and an FEI Scios 2 Dual Beam FIB/SEM. Sub-surface morphology was investigated with transmission electron microscopy (TEM) using a JEOL 2010 LaB_6 TEM operated at 200 kV and a Thermo Themis Z Advanced Probe Aberration Corrected TEM/STEM operated at 300 kV with Bright Field (BF) and High Angle Annular Dark Field (HAADF) imaging. STEM-EDS was performed with this instrument using the FEI Super-X, 4-crystal EDS detection system. Specimens were prepared for TEM analysis via FIB-lift-out method, as well as mechanically scraping fuzz tendrils onto a methanol-soaked lacey carbon TEM grid. Micrograph analysis was performed in ImageJ image analysis software and error measurements on lengths extracted from micrographs represent the standard deviations of multiple measurements [39]. XPS measurements were performed with the in-situ x-ray source (Specs XR-50, Al anode) and hemispherical energy analyzer (Specs EP-150) at the University of Illinois.

3. Results

All exposed samples developed some type of surface nanostructuring under irradiation. **Table 2** outlines the observed surface morphology on all exposed samples. **Figure 1a-b** show the He-induced nanostructuring that developed on the W-1TiC_He specimen. The damage varies across the sample surface, as some regions have pores, while most regions have a short, tendril-like morphology. The cause for the spatial variation of the different nanostructures is unclear at this time. Pores on the surface of some grains have an average diameter of 24 ± 11 nm. FIB investigations show that the thickness of this tendril layer, where present, is ~360 nm. Sub-surface pores are also observed in the regions of tendril development, with these pores being 74 ± 47 nm in diameter, and extending up to ~100 nm beneath the surface. TEM investigations of FIB lift-out samples and fuzz tendrils were carried out separately. TEM analysis conducted

on the tendrils scraped off the surface in **Fig. 1c** shows 30±8.5 nm diameter tendrils, with a large number of He bubbles with an average size of 8.4 ± 5.6 nm present within the tendrils.

Analysis of a bulk lift-out sample in **Fig. 1d** from a region of the sample with surface pores but no fuzz shows large, faceted voids in the subsurface, from 5-50nm deep. In addition to the large voids, small, spherical bubbles are also observed. The STEM-HAADF micrograph and corresponding STEM-EDS map in **Figure 2a-b** shows TiC dispersoids on the scale of 10-100 nm are observed beneath the surface but not directly at the surface. No He bubbles are observed in direct contact with these dispersoids. The average size of faceted bubbles is 11.7 ±5.4 nm, while the average size of the spherical bubbles is 3.0 ±0.9 nm. No association of He bubbles with the TiC dispersoids is observed.

On the W-1TiC_He+HHF specimen, similar surface nanostructure development is observed, as shown in **Fig. 3a-b**. Pores with an average size of 10.8±4.5 nm are observed on the specimen surface and in the sub-surface. Pores in the subsurface are 45.6±34.1 nm nm in diameter, and the porous layer extends ~361 nm beneath the surface shown in **Fig. 3b**. Some grains in **Fig. 3a** show ripples, others show bumps, and others pores, indicating a grain orientation dependence on the nanostructuring. TEM analysis of a lift-out sample in **Fig. 3b** shows the presence of bubbles just beneath the surface. The bubbles have an average size of 45.6±34.1 nm, showing that the sizes have a wide distribution and vary between faceted and spherical bubbles.

Figure 4a shows the surface layer developed on the W-1TaC_He specimen. FIB and TEM analysis indicates that this layer is ~163 nm thick. This fuzzy layer has sub-surface pores underneath up to 500 nm deep, with the pores 55.1±33.0 nm in diameter. TEM analysis of a lift-out sample shows this porous surface layer full of He bubbles in **Fig. 4a.** The bubbles have an average diameter of 3.3 ±1.8 nm, and are almost all spherical. The STEM-HAADF micrograph and corresponding STEM-EDS analysis of the specimen in **Fig. 4b-f** shows that this layer is not W: it is rich in Mo, Fe, and Ti, and has a much lower W concentration than the bulk. The Ti is thought to come from cross-sputtering from the W-1TiC specimen which was

exposed simultaneously, while the Mo and Fe are thought to come from the sample holder and vacuum vessel, respectively.

Adding in the HHF resulted in a coral-like layer as well on the W-1TaC_He+HHF samples, shown in **Fig. 5a-b**. The coral-like layer is ~220 nm thick with sub-surface pores underneath that are 35.2 ±22.1 nm in diameter. Cracks shown in **Fig. 5c-d** were observed on one part of the specimen surface only, resulting in micron-sized cracks.

A Mo-rich impurity layer was observed in STEM-EDS analysis of the sample, indicating that the surface structures formed during irradiation were caused by the Mo deposition. **Figure 6a-c** shows that the surface coral-like layer is not W, but Mo impurities deposited during irradiation. Nonetheless, He bubbles are observed within the Mo impurity layer and at the impurity layer-bulk interface. Bubbles that are at the interface or slightly within the specimen bulk have an average size of 5.4 ±3.7 nm while those in the Mo layer have a wider size distribution and are about 2x larger and can be seen in the scraped-off tendrils. In addition to bulk TEM analysis, scraped-off tendrils were examined in the TEM. **Figure 7** shows 41±16 nm-wide tendrils filled with bubbles with an average size of 9.2 ±5.8 nm indicating that small He bubbles still formed within the Mo impurity layer. In the virgin sample, the He bubbles are smaller than in the impurity layer and there is no morphology present: the virgin surface is flat, with no visible roughening. This shows that despite the He fluence it received before the development of the impurity layer, the bubbles are small and did not accumulate into large grain boundary bubbles, and no surface nanostructuring. Therefore, despite the development of the impurity layer, the dispersoids were able to minimize the He-induced damage.

As shown in **Fig. 8a-b,** the W-5TiC_He+HHF specimen was the only specimen to develop thick, interlocking fuzz tendrils. The fuzz layer is ~400 nm thick and tendrils are 29.6±7.0 nm wide. No presence of TiC dispersoids is observed on the surface as fuzz tendrils cover the entire surface. Bubbles are observed in the subsurface with an average diameter of 10.8±6.8 nm and extend ~60 nm beneath the surface. Bubbles within the tendrils are 9.9±4.9 nm in diameter. STEM-EDS analysis of the lift-out specimen and tendrils

in **Fig. 9a-b** show that the tendril composition is W, with Ti not observed above the background. Further analysis of a bundle of tendrils has shown no preferential spatial enhancement of Ti. Analysis of the tendrils shows that no Ti peaks are observed in the EDS spectra and the Ti concentration is not above the background. It is clear that the tendrils on this specimen are not enriched in Ti and are pure W. Therefore, the He-induced W nanostructures overtake surface TiC dispersoids at high fluences. Nonetheless, the thickness of the nanostructured layer is much less than expected and much less than observed on W specimens under similar irradiation conditions, indicating that the dispersoids had an effect on limiting the nanostructure thickness due to trapping He and limiting He bubble formation in the W matrix, as to be discussed in the Discussion section.

Interestingly, as the dispersoid concentration is increased to 10 wt.% for both TaC and TiC, the specimens had a thick impurity layer deposited on the top surface. This is observed in both the He-only and He+HHF cases. In the He-only case, a translucent layer is apparent in plan-view SEM micrographs, and STEM-EDS confirms the presence of a Mo and Fe-rich surface layer. **Figure 10a** shows the W-10TiC specimen indicating the development of surface nanostructuring, due to the presence of the impurity layer. **Fig. 10a**, however, shows that the TiC dispersoids (appearing black in the micrograph) have a similar size and distribution as pre-irradiation condition, indicating the stability of the dispersoids and that only the surface is altered by the deposition of the impurity layer. TEM analysis of the W-10TiC_He+HHF specimen in **Fig. 10b-f** shows large, faceted bubbles are observed in the ~1.6 μm thick impurity layer with an average size of 10.5±5.5 nm. STEM-EDS confirms the presence of a Mo/Fe impurity layer on the W-10TiC_He+HHF specimen

On the W-10TaC specimen, the deposited layer took the form of terraced structures, on the W-10TaC_He and W-10TaC_He+HHF specimens. This development of He bubbles within the impurity layer is confirmed with TEM/STEM investigations in **Fig. 11a-b**. The W-10TaC_He specimen shows the development of a ~80 nm thick impurity layer, confirmed via EDS investigations. However, within this layer He bubbles are observed with an average diameter of 2.9±1.5 nm showing that He bubbles formed within this layer.

4. Discussion

It is clear that the dispersion-strengthened W did not completely prevent the formation of surface nanostructures, but may have suppressed nanostructuring, although the intricacies of the relationship are difficult to ascertain due to the development of the surface impurity layer. Surface impurity layers have been deposited on specimens exposed in other linear plasma devices around the world, indicating that this is not an issue purely relevant to Magnum-PSI [40]. In fusion reactors, erosion, migration, and re-deposition of material occurs on a large scale resulting in altered surface compositions and chemistries that will change the material surface response to the plasma and subsequent plasma behavior [41-46]. The composition of the impurity layer formed in these experiments in Magnum-PSI mirrors the metals of Ni, Cr, Fe, Cu, and Mo that have been experimentally seen in re-deposited layers in the DIII-D tokamak [47].

The composition of the layer on specimens examined here was mainly Mo and Fe, attributed to cross-sputtering from the source and Mo sample holder used during the experiments. Spectral analysis (not shown) of the atomic emission lines tracked during the irradiation show a greater intensity of Fe and Mo emission lines throughout the irradiation compared to W, and Fe and Mo lines are particularly intense at the end of the irradiation. Thus, the Fe and Mo impurity layer formed during the irradiation process, but the virgin sample surface was exposed to some He fluence prior to significant impurity layer formation. XPS investigations (not shown) also confirm the presence of Mo, Cu, and Fe on the specimen surface, and the presence of Ti/Ta is not observed at all after light sputtering.

Additionally, the FIB micrograph shows that beneath the impurity layer, the dispersoid microstructure still exists, so the material bulk is still stable and has the same microstructure and likely the same bulk mechanical properties as pre-irradiation. This is an important qualification, as it demonstrates that the entire material bulk is not affected and the bulk properties for which the dispersion-strengthened materials are desired are not detrimentally impacted by the development of a surface co-deposited impurity layer, an important result for employing these types of materials in a future reactor environment.

The experiments performed here nonetheless show that even as impurity layers accumulate on top of W surfaces, He bubbles will still form within the re-deposited layer. After some time in a tokamak, incident He ions will no longer interact with a virgin PFC surface, but rather a mixed-material surface. This is an important result, showing that the behavior of He with mixed materials may be more relevant than further studies on pure W. The size and density of bubbles is affected by the presence of the impurity layer, and are certainly affected by the presence of synergistic high heat flux pulses to be discussed later. The bubbles within the impurity layer are larger than in the bulk attributed to the dispersoid inclusion. Samples that developed a nanostructure layer while also having bubbles in the virgin specimen, the average bubble size in the impurity layer is larger than in the bulk, attributed to the presence of the dispersoid microstructure. The He bubble concentration may not be high enough in the impurity layer for the transition to nanostructure formation to occur, while the irradiation temperature and fluence indicate that nanostructures should form. Thus, the impurity layer, particularly with the synergistic HHF, has less nanostructure development than expected, perhaps due to the intrinsic porosity of this layer and high density of free surfaces. Faceted bubbles were still observed on some specimens in the re-deposited layer, indicating that faceting is not a feature limited tungsten or other bulk, polycrystalline materials.

On specimens that did not have the development of an impurity layer, the nano-fiber fuzz layer is only ~360 nm thick, much less thick than pure W specimens exposed to similar plasma conditions. According to T. Petty, et al. at ~1273 K, a fuzz thickness of ~1 μm can be expected to form at these temperatures and fluences [48]. Additionally, the roadmap developed by El-Atwani, et al. show that under these conditions a nano-tendril layer should form, and prior experiments on ultra-fine grain W show ~1μm thick fuzz layer [11]. Calculations of the expected fuzz layer thickness consider the He diffusion rate, temperature, and ion fluence. While this is merely a guide, our observations significantly differ from the expected layer thickness.

The stunted nanostructure growth may be attributed to the presence of second phase dispersoids or the surface impurity layer. The impurity layer that deposited on top of the specimens during irradiation undoubtedly captured He atoms (as evidenced by the He bubbles within these layers) and prevented them

from reaching the W bulk, thus limiting the potential for He bubble formation in W and subsequent W nanostructure formation. A second factor affecting the stunted growth of the W fuzz layer may be sputtering due to the heavy metal deposition. While the incident He ions were below the W sputtering threshold, the sputtering threshold for Mo and Fe on W are much lower, and SRIM calculations indicate that 30 eV Mo and Fe ions can induce sputtering of W and Ta/Ti. Thus, incident Mo and Fe ions from the plasma device may have sputtered specimen surface atoms before depositing on the surface stunting the growth of fuzz.

The pores on the W-1TiC_He specimen mirrors a result by Donovan, et al. showing the bursting of He bubbles at the surface and presence of pores on the surface [49]. This shows that 1) He bubbles were formed in the specimen and were mobile at high temperatures to diffuse to the surface, and 2) the bubbles were over-pressurized and ruptured at the surface. The bursting of bubbles may eject W dust and may cause issues for reactors. The sizes of the bubbles within the sub-surface and tendrils agree with prior literature on the subject, but there is no grain orientation dependence on the tendrils observed. Although, there is a grain orientation dependence on the nanostructuring observed on the W_1TiC_He and He+HHF specimens, which agrees with observations by D. Donovan, et al on pure W under similar exposure conditions [49].

While the dispersoids did not prevent fuzz formation, they may have limited nanostructure growth due to the presence of carbide dispersoids, as carbon and oxygen interactions with W have shown to limit He nanostructuring [50, 51]. Compared to models of fuzz thickness on pure W, the nanostructure thickness on DS-W is less than expected, however no clear trend is observed, as increasing the dispersoid content does not directly correlate to a reduction in the nanostructure thickness, as the W-5TiC_He+HHF sample develops only ~400nm thick fuzz, while pure W is predicted to develop microns-thick fuzz. Due to the development of impurity layers on the 10wt.% samples, the He interactions with high dispersoid contents cannot be easily determined at the high fluence. We can determine from this study that the dispersoids have an effect on the He interactions at low fluence before the impurity layer formed. Therefore, the dispersoids do limit He bubble formation.

The different dispersoid types also did not significantly affect the size of tendrils, sub-surface He bubbles, or intra-tendril bubbles. The size of the bubbles beneath the impurity layer is similar, irregardless

of the dispersoid composition. However, the mere presence of the dispersoids has an effect to limit the He bubble formation due to their carbon-oxygen-metal composition. Carbon seeding in the plasma and pre-irradiation with carbon atoms have both been shown to reduce fuzzy nanostructure growth on pure W surfaces. A. Al-Ajlony, et al. studied the effect of C pre-irradiation on fuzz growth, noting that pre-irradiation stunted the He nanostructure growth [50]. Additionally, plasma seeding with C results in a C layer on the surface that affected W nanostructure growth [51]. Thus, carbon pre-existing in the sample may have the same effect to limit nanostructure growth.

No preferential trapping of He bubbles at dispersoid-W boundaries is observed, contrary to expectations. Preferential trapping of He at carbides have been observed in steels [52-55]. In-situ work done with Kr irradiation of W-1.1TiC materials demonstrated biased sink behavior of the TiC dispersoids as large voids were observed at the dispersoid-tungsten interface. The improved radiation resistance of the alloy was attributed to enhanced defect annihilation and decreased loop mobility due the dispersoids [55]. The Kr^+ damage done by El-Atwani, et al. is not a direct comparison as the 1 MeV Kr^+ used for irradiation will induce knock-on damage while the 35 eV He^+ will not, so different mechanisms governing damage production are to be considered.

In the work presented in this manuscript, no large voids were found at TiC dispersoids and no preferential trapping at the carbides was observed either. In the work by Edmondson, et al. [52] the He bubbles were preferentially formed at Ti(N,C) precipitates and matrix grain boundaries after 335 keV He irradiation, above the knock-on damage threshold. The authors noted the interactions between vacancies, O and He atoms that may cause the preferential trapping [52] and B. Mazumdar noted the strong He-C bonds that may influence preferential trapping at carbide precipitates [53]. Additionally, faceted bubbles were observed after a $6.75x10^{21}$ m^{-2} fluence [52]. In the DS-W samples examined here, there is likely a similar interplay between the He, vacancies, and O influencing He behavior.

. According to the roadmap provided by El-Atwani, et al. the tempeartures and fluences examined here should create a fuzz layer on W [11]. Indeed, even an ultra-fine grained W samples with a high grain boundary density showed thick tendrils at similar irradiation conditions. Therefore, it is clear that the DS-

W samples examined here have limited nanostructure formation. Despite the impurity layer, the virgin DS-W sample received some He fluence prior to the impurity deposition. Despite this, there is much decreased bubble size and density and resulting surface morphology than would be expected. The samples that developed an impurity layer show very few He bubbles beneath the layer, and no bubble accumulation at W-W grain boundaries, which may impact the material properties. It is asserted that due to the presence of the dispersoids altering the interface chemistry and trapping He in small clusters, He bubble nucleation, growth, and segregation to grain boundaries is limited.

The lack of visible bubbles seen within the dispersoids or at the W-dispersoid interfaces, may not indicate the He is not being trapped at the disperosids. The dispersoids in the DS-W materials in this study are not pure carbides, and have a mixed metal-oxygen-carbon stoichiometry [56]. Helium is observed to be trapped atomically in oxygen-implanted regions of titanium, and ZrO_x and TiO_x have been shown to have He bubble damage response dependent on the oxygen concentration [57-60]. Additional evidence for trapping of He in small clusters, potentially TEM-invisible bubbles, is proposed via first-princioles studies of He interactions with TiO_2 in Fe matrices: increased trapping at the dispersoids depended on the oxygen content within second phase particles [61]. Titania dispersoids in Fe have a higher binding energy and allow for less He bubble formation, and a similar effect may be occurring in the W-TiC dispersoids, as TiO_2 has a lower He binding energy and higher He migration threshold than W, so He trapped at TiC dispersoids (which have a mixed metal-oxy-carbide composition) may be trapped and not form visible bubbles [61, 62]. The lack of bubbles at W-dispersoid interfaces may be attributed to semi-coherent metal-oxide interfaces better tolerating radiation-induced defect damage than metal-metal interfaces, attributed to the interface stoichiometry [63]. We assert that a combination of these effects is occurring here, as the second phase dispersoids have a mixed metal-oxygen-carbon composition, and the interfaces with W are not metal-on-metal, resulting in altered He bubble dynamics. The dispersoids in this study have a non-stoichiometric composition, and therefore the oxygen content has an effect on the He trapping and bubble formation within the dispersoids. Subsequent He trapping in the dispersoids means that less He is available for trapping in W grains, which would then lead to the smaller bubbles and less thick surface morphology observed on the

DS-W specimens. To best confirm these assertions, Atom Probe Tomography (APT) investigations will be undertaken to observe if TEM-invisible He bubbles are indeed accumulating at the carbide dispersoids.

The tendril compositional analysis shows that the tendrils are pure W. At the dispersoid concentrations studied at these He fluences, when nanofeatures form, they are W in composition. As the irradiation progressed, the surface evolved from a mix of W and TiC to W-only nanostructures, therefore, in a similar fashion to the samples that had impurity layer deposition, this result indicates that in a fusion reactor the starting material surface will be altered during operation. The surface composition will be reconstituted throughout plasma discharges, altering the surface composition, morphology, and plasma response.

One must also consider the inclusion of the high heat flux pulsing. The lack of significant cracking agrees with results observed by Buzi, et al. showing the development of micron-sized cracks in a localized area on pure W under simultaneous He exposure and pulsed laser heating at Magnum-PSI [64]. Droplet formation was not observed, nor was there a significant reduction in fuzz layer thickness that may be expected if the HHF pulses were expected to have an annealing effect on the fuzz. However, as De Temmerman, et al. note [65], an equilibrium fuzz thickness will be reached after simultaneous He+ELM exposure. However, in an ELM event, the heat fluxes will be combined with high energy particle fluxes, which are not modelled in these experiments. In simulations utilizing similar ELM frequency, duration, and heat flux parameters as these experiments, a nanostructured layer that is hundreds of nanometers thick is expected to develop on a W surface. The presence of small grains in the near-surface is under investigation by laser-only HHF-simulated pulses to isolate the effects of ELM-like temperature excursions on the microstructure to understand if this indicates the beginnings of HHF-induced recrystallization.

Grain detachment is observed as well, a result mirrored by others, such as El-Atwani, et al [66]. This is likely due to the addition of the HHF causing grain de-cohesion. Surface roughening has been observed after HHF loading, but the specific grain de-cohesion may be attributed to weakened grain boundaries due to the presence of He atoms at the grain boundaries. Grain boundaries have been shown to be He traps and not high diffusion pathways [16, 67]. Additionally, the accumulation of He atoms at the

grain boundaries weakens grain cohesion [68]. Although He bubbles were not observed at grain boundaries, He atoms can still segregate to grain boundaries to decrease grain cohesion and not be visible in the TEM.

Under sequential He+HHF exposures at lower He fluences, G. Sinclair et al. observed the development of a shale-like morphology and reduced surface morphology development [34]. Additionally, application of laser pulses at Pilot-PSI after formation of a W fuzz layer resulted in diminishment of the surface morphology as the laser power increased [31]. A power density of 0.1 MJ m^{-2} did not alter the fuzz layer, but 0.5 MJ m^{-2} completely removed the fuzz layer. Simultaneous He+HHF loading on pure W resulted in W droplet development and significant surface pore formation [31]. Y. Hamaji, et al. also observed similar morphology after sequential He+HHF exposure: a flattened surface morphology and reduced sub-surface bubble density was observed after exposure to 500 MW m^{-2} heat fluxes [32]. In this study, there is an additional effect of the laser pulsing: in the impurity layers formed on samples without the HHF pulsing, the average bubble diameters are 2.9±1.5 nm and 3.2±1.8 nm, while the average bubble diameters in the impurity layers of samples that experienced the HHF pulses are 10.5±5.5 nm, 35.2 ±22.1 nm, and 45.6±34.1 nm. Also, the bubble density in the impurity layer is ~4x lower on the He+HHF samples. Thus the bubbles on the samples that experienced synergistic HHF pulsing are larger and less dense than those that formed in the impurity layer under quiescent He irradiation indicating that the HHF results in the coalescence of bubbles due to the temperature excursion, and only affects bubbles in the first 100's of nm's, or the thickness of the impurity layer. This shows that in a reactor, the co-deposited impurity layer will have bubble morphology that is affected by high heat flux pulses. Additionally, the combined high heat flux contributed to a lower bubble density, which can result in less nanostructure formation, and indeed no nanostructuring on the surface of the impurity layer is observed.

The lack of cracking on most samples can be attributed to the enhanced ductility of these materials compared to monolithic W. The fuzz layers that developed were not stunted on the HHF-exposed samples, and in fact the thickest fuzz layer was observed on the W-5TiC_He+HHF specimen. This indicates that the fuzz layer still forms on specimens with synergistic HHF pulses, and that the nanostructures are stable under HHF loading. This is an important result, as the structural stability of the fuzz layer must be maintained to

limit material erosion and injection into the core plasma. This is important result may raise the operating window for W alloys and improve the viability of DS-W material performance in a reactor environment.

5. Conclusions

The behavior of dispersion-strengthened W materials under low energy, high flux He irradiation has been studied with and without synergistic high powered laser pulses. As outlined in **Table 2,** exposures to pure He plasmas resulted in the formation of surface nanostructures on W-1TiC and W-1TaC specimens, taking the form of pores and ripples and coral-like layers ~300 nm thick. However, STEM-EDS investigations show that the surface nanostructured layer is primarily composed of re-deposited Mo and Fe, impurities from the plasma source and sample holder. Spherical and faceted helium bubbles are observed in the impurity layer and up to ~50 nm beneath the impurity layer in the specimen bulk. W-10TiC and W-10TaC specimens show the development of a thick impurity layer as well. Within this Mo-rich layer, He bubbles are observed. Only the W-5TiC specimen showed the development of W fuzz tendrils, with ~400 nm thick tendrils filled with He bubbles. Simultaneous HHF pulsing caused the development of cracks on only the W-1TaC_He+HHF sample and did not significantly alter the resulting surface morphology, indicating structural stability of the nanostructure and potential cracking resistance of the dispersion-strengthened materials. The development of the surface impurity layer mimics the surface that will be formed in the divertor region of fusion reactors, as erosion and re-deposition will result in a mixed material layer with a composition that differs from the bulk material. Thus, the PMI response to the mixed material layer in these studies allows for a comparison to the response in fusion reactors, potentially motivating the need to study mixed material systems or impurity-rich material layers rather than pure W, for example, to best understand how He may behave with the divertor surface in future fusion reactors.

The dispersion-strengthened materials did not inhibit surface nanostructure formation, although the development of the surface impurity layer does obscure conclusions about the specific He-dispersoid interactions. However, due to the formation of surface nanostructures on 1 and 5wt.% samples, it is concluded that at the high fluences examined, He-W interactions dominate over He-dispersoid interactions,

which lead to the development of W nanostructuring. Preferential He bubble trapping at the carbide dispersoids is not observed, but finer examinations may elucidate their behavior. Under high fluence, reactor-relevant He exposure, the behavior of dispersion-strengthened W mirrors that of pure W, as surface nanostructuring will develop, and the mitigating the erosion of these nanostructures must be the focus of future studies.

Acknowledgements

The characterization was carried out in part in the Frederick Seitz Materials Research Laboratory Central Research Facilities, University of Illinois. This work is supported by US DOE Contract No. DE-SC0014267.

References

[1] Y. Ueda, et al. *Nucl. Fusion* **57** (2017) 092006.
[2] R.A. Pitts et al. *J. Nucl. Mater.* **438** (2013) S48–S56.
[3] E. Lassner and W.D. Schubert. Tungsten: Properties, Chemistry, Technology of the Element, Alloys, and Chemical Compounds. Kluwer Academic. Plenum Publishers. New York, NY. 1999.
[4] S.J. Zinkle, et al. *Fusion Eng. Des.* **51–52** (2000) 55–71.
[5] S.J. Zinkle, et al. *Annu. Rev. Mater. Res*. 2014. 44:241–67
[6] S. Kajita, et al. *Nucl. Fusion* **49** (2009) 095005.
[7] M Miyamoto, et al. *Phys. Scr*. **T159** (2014) 014028
[8] M. Baldwin, et al. *Nucl. Fusion* **48** (2008) 035001.
[9] D. Nishijima, et al. *J. Nucl. Mater*. **329–333** (2004) 1029–1033.
[10] H. Iwakiri et al. *J. Nucl. Mater.* **283-287** (2000) 1134-1138.
[11] O. El-Atwani, et al. *Nucl. Fusion* **54** (2014) 083013.
[12] S. Zenobia, et al. *J. Nucl. Mater.* **425** (2012) 83-92.
[13] F. Meyer, et al. *J. Physics: Conference Series* **488** (2014) 012036.
[14] L. Liu et al. *J. Nucl. Mater.* **471** (2016) 1-7.
[15] K. Wang, et al. *Sci. Rep.* **7**, 42315; doi: 10.1038/srep42315 (2017).
[16] K. Wang et al. *Acta Materialia* **124** (2017) 556-567.
[17] D. Dasgupta, R.D. Kolasinski, R.W. Friddle, L. Du, D. Maroudas, and B.D. Wirth. *Nuclear Fusion* **59** 8 (2019).
[18] F Sefta, et al. *Nucl. Fusion* **53** (2013) 073015 (7pp).
[19] S. Sharafat, et al. *J. Nucl. Mater.* **389** (2009) 203–212.
[20] S. I. Krasheninnikov. *Phys. Scr*. **2011**(2011) 014040.
[21] Y. Kim, et al. *Int. J. Refractory Metals & Hard Mater*. **27** (2009) 842–846.
[22] D. Lee, et al. *Int. J. Refractory Metals & Hard Mater*. **44** (2014) 49–53.
[23] H. Kurishita, et al. *J. Nucl. Mater*. **398** (2010) 87–92.
[24] Y. Ishijima, et al. *Mater. Sci. & Eng. A* **473** (2008) 7–15.
[25] H. Kurishita, et al. *Mater. Sci. & Eng. A* **477** (2008) 162–167.
[26] H. Kurishita, et al. *Adv. Mater. Research* **Vol. 59** (2009) 18-30.
[27] H. Kurishita, et al. *Phys. Scr*. **T128** (2007) 76–80.
[28] M.J. Baldwin, et al. *J. Nucl. Mater*. **404** (2010) 165–173.
[29] M. Yamagiwa et al. *J. Nucl. Mater.* **417** (2011) 499–503
[30] X. Liu, et al. *Nucl. Mater. & Energy* **12** (2017) 1314–1318.
[31] G. De Temmerman, et al. *J. Nucl. Mater.* **88** (2013) 483-487.
[32] Y. Hamaji, et al. *Nucl. Mater. & Energy* **18** (2019) 321–325
[33] L. Buzi et al. 2017 *Nucl. Fusion* **57** 126009.
[34] G. Sinclair et al. *J. Nucl. Mater.* **508** (2018) 26-32.
[35] E. Lang, et al. *Int. J. Refractory Metals & Hard Mater.* **75** (2018) 279-286.
[36] G. De Temmerman et al. *Fusion Eng. Des.* **88** (2013) 483–487.
[37] H.J.N. van Eck, et al. *Fusion Eng. Des.* **142** (2019) 26-32.
[38] H.J.N. van Eck, et al. *Fusion Eng. Des.* **89** (2014) 2150–2154.
[39] J. Schindelin, et al. *Nature Methods* (2012) **9**(7): 676-682, PMID 22743772, doi:10.1038/nmeth.2019.
[40] D. Nishijima, et al. *Nuclear Materials and Energy* **18** (2019*)* 67–71.
[41] C. Hu et al. *Fusion Eng. Des.* **112** (2016) 117–122
[42] J.N. Brooks *et al* 2009 *Nucl. Fusion* **49** 035007.
[43] A. Hakola *et al* 2017 *Nucl. Fusion* **57** 066015.
[44] M. Tokitani et al. *J. Nucl. Mater.* **438** (2013) S818–S821 S819
[45] R. Ding, et al. *Nucl. Mater. & Energy* **12** (2017) 247-252.
[46] V.K. Gusev, et al. *Nucl. Fusion* **49** 2009 (6pp).

[47] C.P. Chrobak, et al. “DIII-D First Wall Metal Impurity Migration Trends,” APS Division of Plasma Physics Meeting 2016, abstract id. PP10.041, October 2016.
[48] T. Petty, et al. *Nucl. Fusion* **55** (2015) 093033 (11pp).
[49] D. Donovan, et al. *Fusion Sci. & Tech.* **72** (2017) 337-346.
[50] A. Al-Ajlony et al. *J. Nucl. Mater.* **466** (2015) 569-575.
[51] M.J. Baldwin, et al. *J. Nucl. Mater.* **390-391** (2009) 886-890.
[52] P. D. Edmondson et al. *Scripta Materialia* **65** (2011) 731–734.
[53] B. Mazumder et al. *Nucl. Mater. & Energy* **1** (2015) 8–12
[54] J Spitznagel, et al. *J. Nucl. Mater.* **122 & 123** (1984) 253-253.
[55] O. El-Atwani, et al. *Acta Materialia* **164** (2019) 547-559.
[56] E. Lang, et al. *Nucl. Mater. & Energy* **19** (2019) 47–54.
[57] J. Matsunaga, et al. *J. Nucl. Sci. & Tech.* **51** (2014) 1231-1240.
[58] G. Valisa, et al. *J. Nucl. Mater.* **402** (2010) 87–92.
[59] Y. Baba, et al. *J. Nucl. Mater.* **152** (1988) 295-300.
[60] M.B. Lewis. *Nucl. Instr. & Methods in Phys. Res.* **B22** (1987) 499-503.
[61] P. Erhart. *J. Appl. Phys.* **111** 113502 (2012).
[62] J.G. Niu, et al. *AIP Advances* **4**, 067128 (2014).
[63] V. Shutthanandan, et al. *Adv. Mater. Inter*. 10.1002/admi.201700037.
[64] L. Buzi *et al* 2017 *Nucl. Fusion* **57** 126009 (10pp).
[65] G. De Temmerman, et al. *Nucl. Mater. & Energy* **19** (2019) 255–261.
[66] O. El-Atwani et al. *Fusion Eng. Des.* **93** (2015) 9–14.
[67] K. Hammond, et al. *EPL* **110 (**2015) 52002.
[68] E. Martinez, et al. *Nucl, Fusion* **57** 2017.

Tables and Figures

Table 1 Outline of irradiation parameters for specimens exposed at Magnum-PSI. Samples named with "HHF" were exposed to high powered laser pulses, with the number of pulses and temperature excursion experienced indicated.

Sample	**He Fluence (m^{-2})**	**Base Temperature (C)**	**ΔT (C)**	**Number of Pulses**
W_1TiC_He	$5x10^{26}$	850-1080	N/A	N/A
W_1TiC_He+HHF	$5x10^{26}$	1150	~250 C	211
W_1TaC_He	$5x10^{26}$	850-1080	N/A	N/A
W_1TaC_He+HHF	$5x10^{26}$	1150	~250 C	211
W_5TiC_He+HHF	$5x10^{26}$	1080	~250 C	53
W_10TiC_He	$5x10^{26}$	900-1100	N/A	N/A
W_10TiC_He+HHF	$5x10^{26}$	800-1050	~250 C	36
W_10TaC_He	$5x10^{26}$	900-1100	N/A	N/A

Table 2 Outline of specimens exposed at Magnum-PSI and corresponding surface morphology that developed after irradiation.

Sample	**Morphology Development**
W_1TiC_He	Ripples, pinholes, proto-tendrils
W_1TiC_He+HHF	Ripples, pinholes, proto-tendrils
W_1TaC_He	Porous impurity layer
W_1TaC_He+HHF	Porous impurity layer
W_5TiC_He+HHF	Thick, interlocking tendril layer
W_10TiC_He	Porous impurity layer
W_10TiC_He+HHF	Porous impurity layer
W_10TaC_He	Porous impurity layer

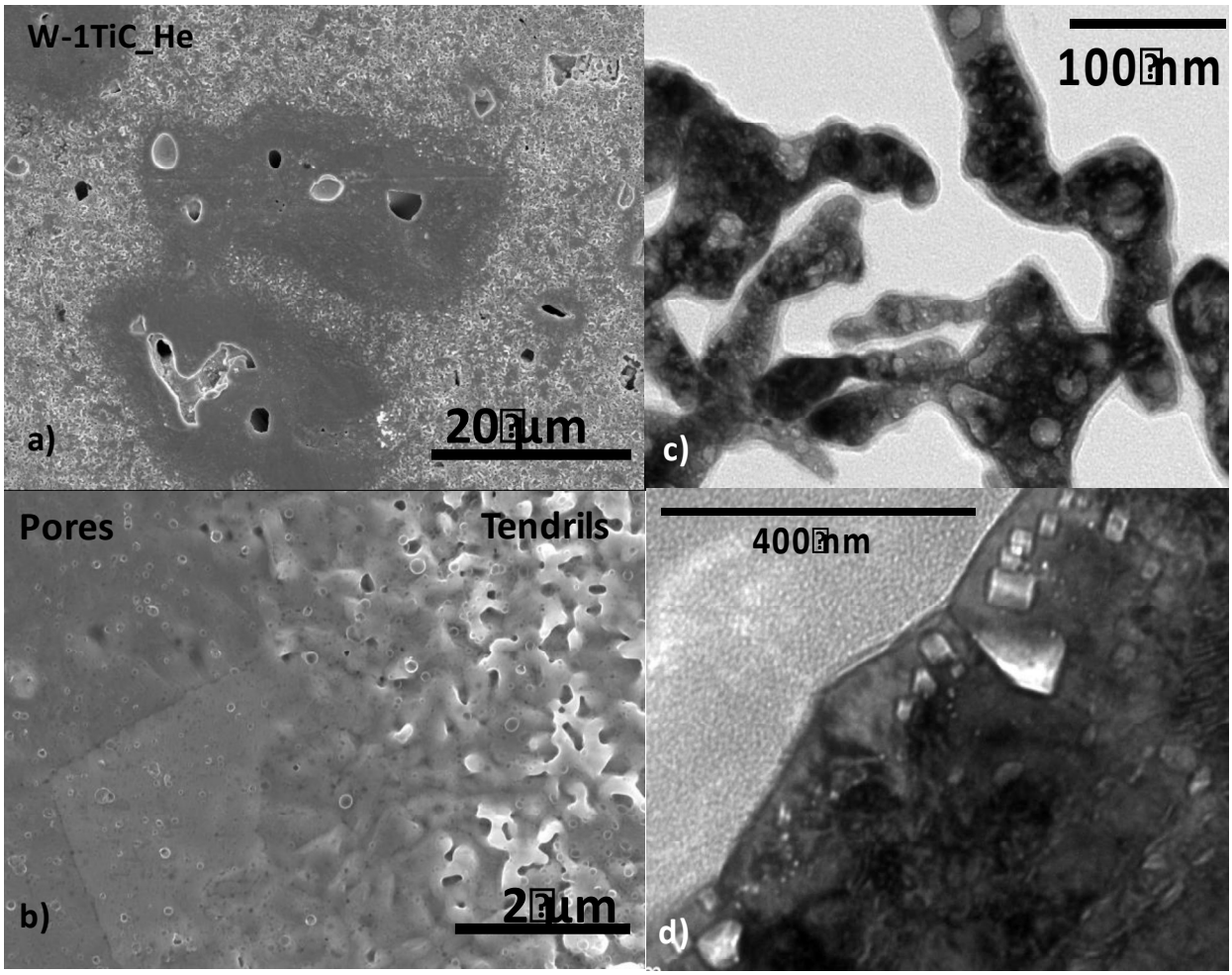

Figure 1 SEM and TEM images of surface morphology developed of W-1TiC_He specimen after He exposure to a $5x10^{26}$ m^{-2} fluence at ~1000 C. SEM images of **(a)** pores (dark regions on surface) and tendrils (light regions on surface) and **(b)** magnified image showing coral-like tendrils observed on part of the surface adjacent to pores. **(c)** TEM micrographs of scraped-off tendrils showing He bubbles within and **(d)** showing faceted He bubbles in the subsurface from the region of the sample with surface pores.

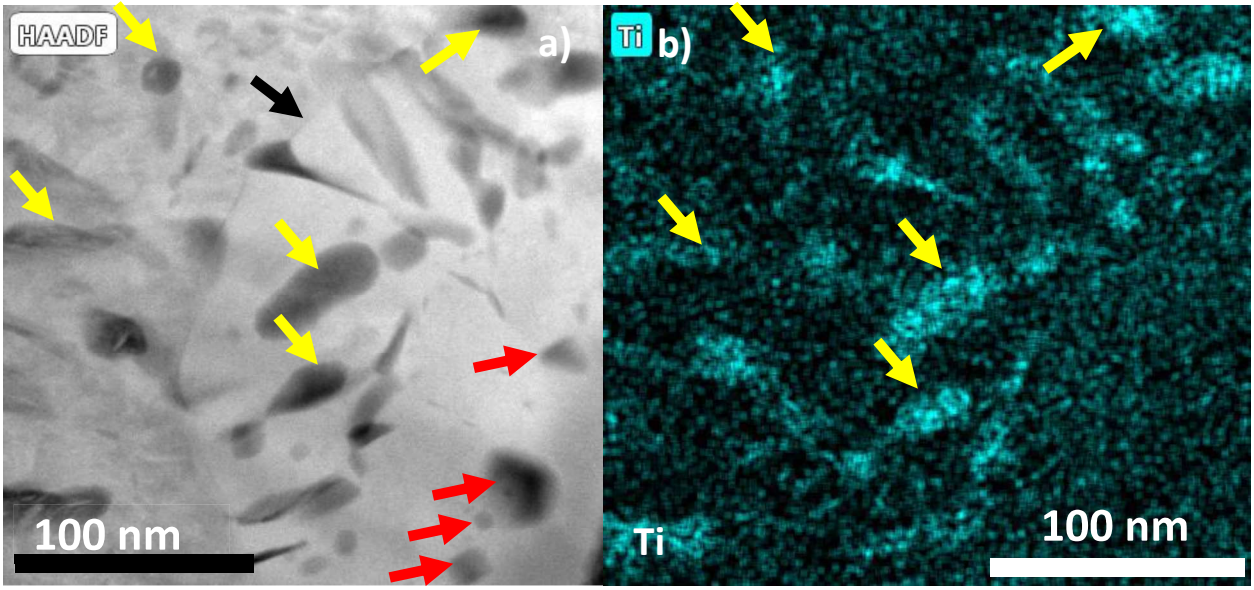

Figure 2 STEM-HAADF micrographs of W-1TiC_He specimen exposed to a $5x10^{26}$ m^{-2} fluence at ~1000 C. HAADF image is shown in **(a)** showing He bubbles with red arrows, yellow arrows denoting some Ti dispersoids, and grain boundary with black arrow. Other gray areas in micrograph are Ti dispersoids, confirmed in the STEM-EDS map shown in **(b)** showing the Ti-rich regions in the sample. EDS mapping is performed with a 3x3 pixel averaging kernel.

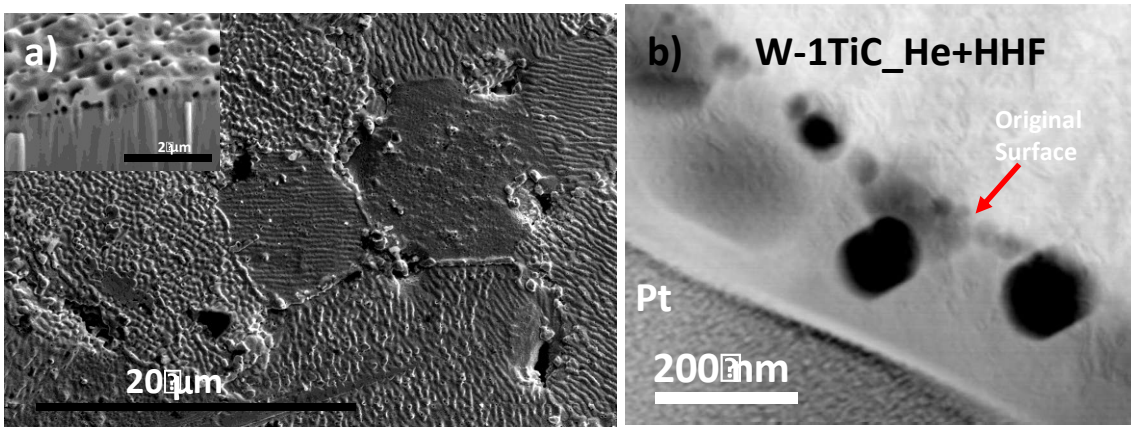

Figure 3 (a) SEM micrographs of surface morphology developed on W-1TiC_He+HHF specimen exposed to a $5x10^{26}$ m^{-2} fluence at ~1100 C with simultaneous laser pulses. Inset shows FIB cross-section of surface showing the sub-surface pores and bubbles that developed during irradiation. STEM-HAADF micrograph in **(b)** shows the presence of He bubbles, many of which are faceted, in the near-surface region (light grey) and the impurity layer (dark grey) consisting of bubbles as well.

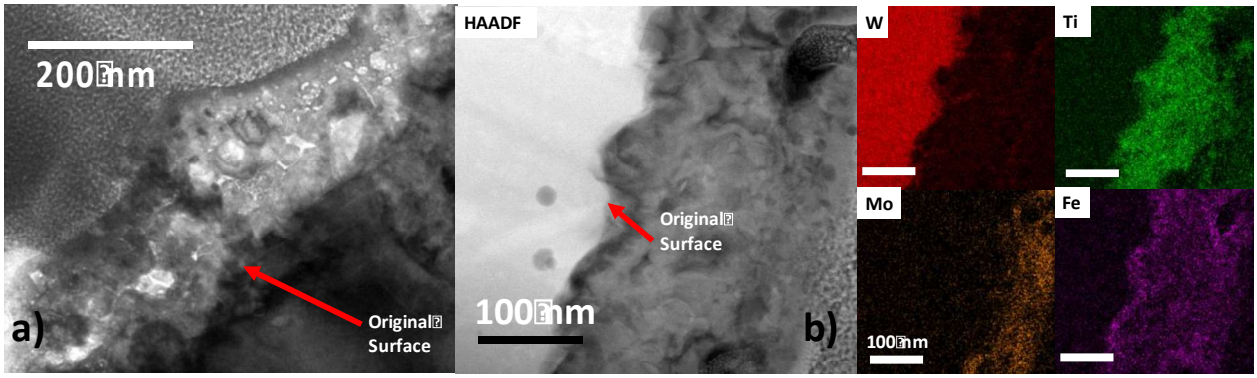

Figure 4 (a) TEM micrograph of W_1TaC_He specimen exposed to a $5x10^{26}$ m^{-2} fluence at ~1000 C showing development of He bubbles within the ~160 nm thick co-deposited impurity layer (light grey) on top of W sample (dark grey). STEM-HAADF micrograph in **(b)** and corresponding STEM-EDS maps of W, Ti, Mo, and Fe show that the surface layer in indeed rich in impurities.

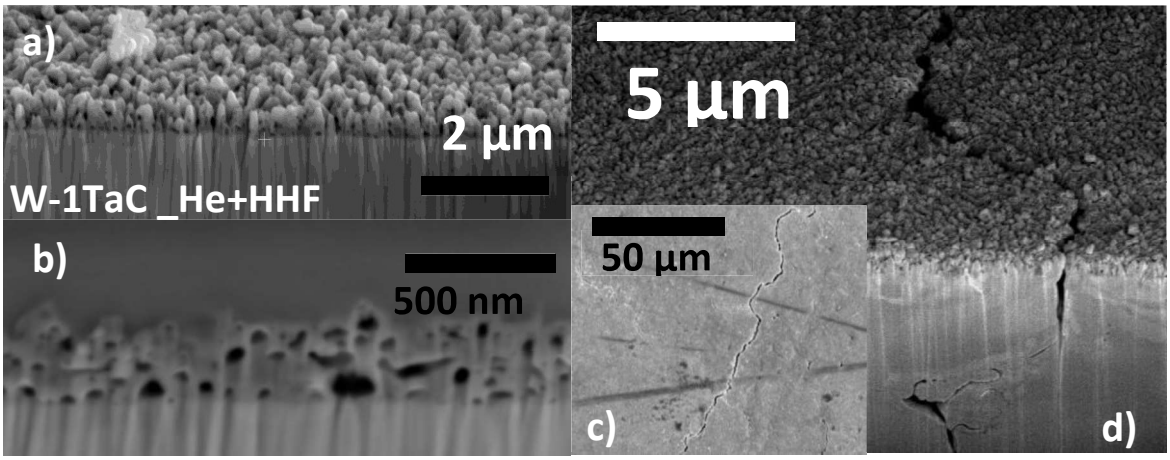

Figure 5 FIB cross-sectional views **(a-b)** of surface morphology formed on W-1TaC_He+HHF specimen exposed to a $5x10^{26}$ m^{-2} fluence at ~1100 C with simultaneous laser pulses. In (b) the surface morphology is encased in platinum used to protect the surface during cross-sectioning. Plan-view (**c**) and FIB cross-sectional view **(d)** of crack formed on W-1TaC_He+HHF specimen. Cracking was not extensive and cracks were 5-1,000 µm long, ~1-3 µm wide, and extended up to ~7 µm deep.

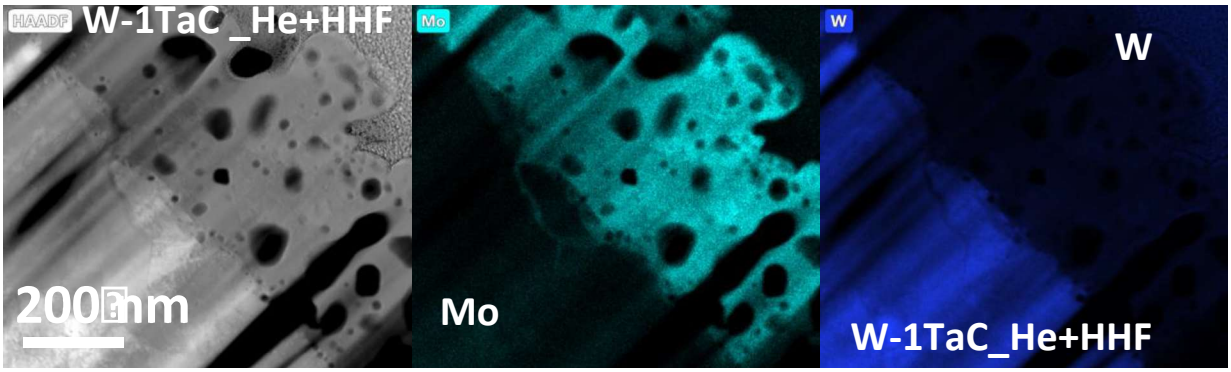

Figure 6 STEM-HAADF micrographs and STEM-EDS maps of Mo and W of the W-1TaC_He+HHF specimen showing the nanostructured layer is a Mo impurity layer. Nonetheless, He bubbles are observed within this layer.

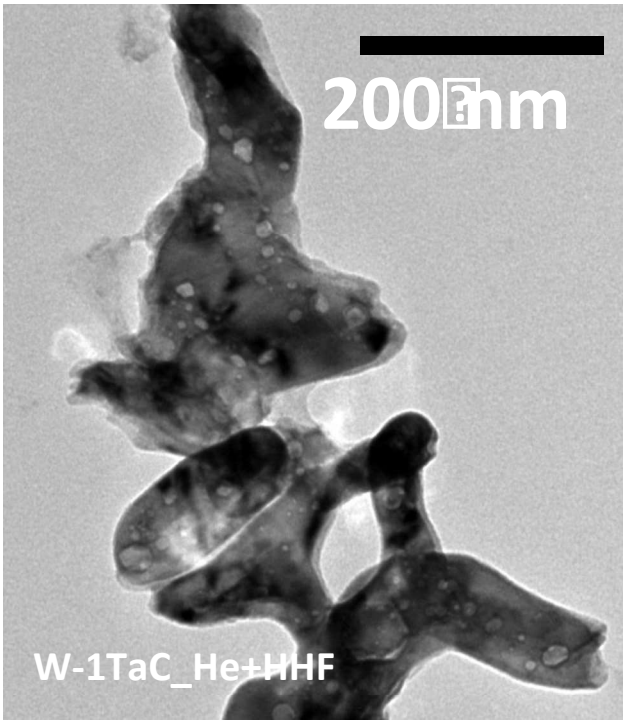

Figure 7 TEM micrograph of scraped-off tendril from W-1TaC_He+HHF specimen showing He bubbles (spherical and faceted) within.

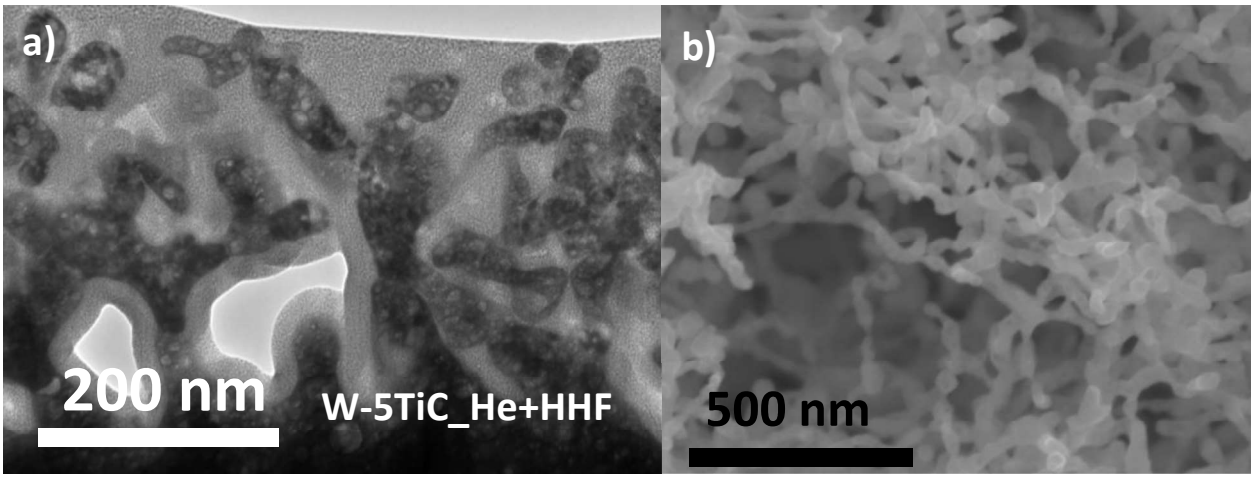

Figure 8 (a) TEM and **(b)** SEM micrograph of fuzz layer produced on W-5TiC_He+HHF sample exposed to a $5x10^{26}$ m^{-2} fluence at ~1100 C with simultaneous laser pulses. Helium bubbles are clearly evident in the fuzz tendrils encased in platinum in (**a**) used during FIB lift-out and in the sub-surface. Fuzz layer is ~400 nm thick and tendrils ~29 nm wide.

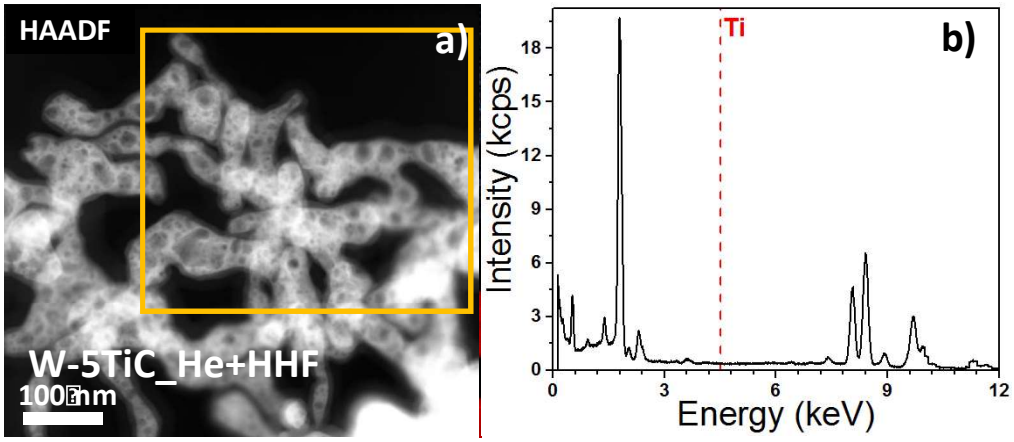

Figure 9 (a) STEM-HAADF micrograph of W-5TiC_He+HHF specimen showing fuzz layer. Corresponding STEM-EDS maps of W and Ti and EDS spectrum of rectangular area in (**b**) indicating no Ti peak and thus likely a pure W tendril composition. EDS maps are shown with 3x3 pixel averaging kernel. No Mo was observed on this specimen.

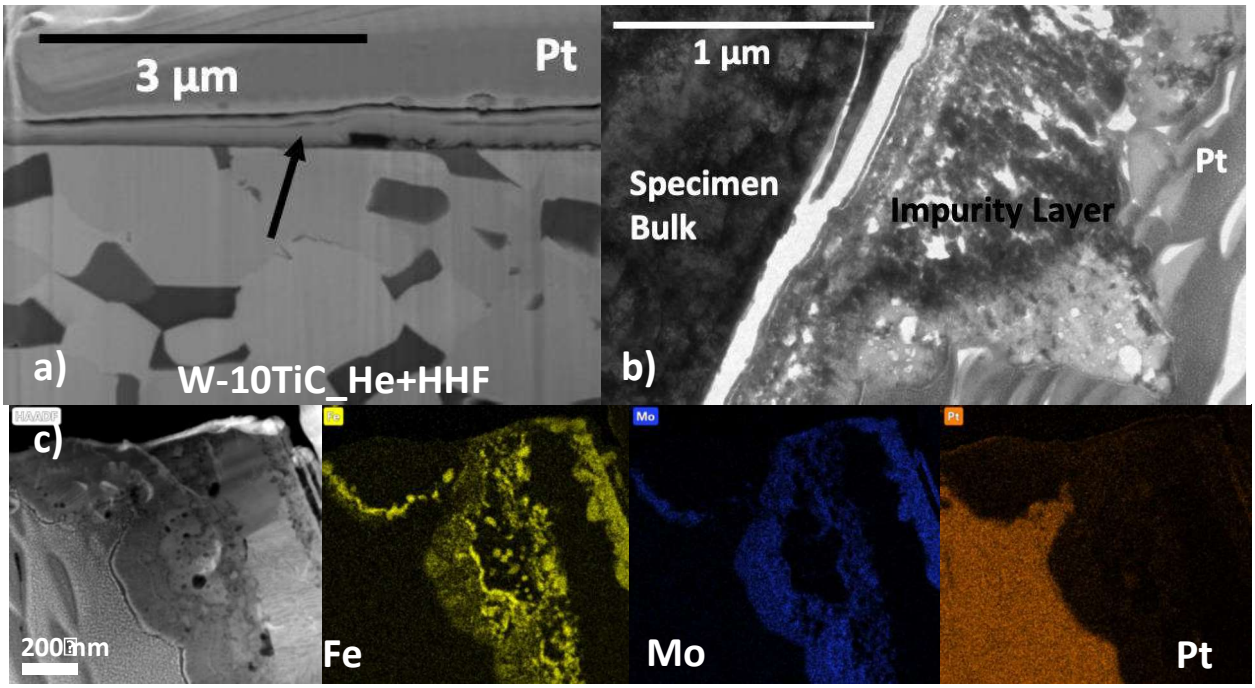

Figure 10 W-10TiC_He+HHF with an **(a)** impurity layer on the surface is denoted with the black arrow in the FIB cross-sectional micrograph while TiC dispersoids appear in black in the micrograph. Helium bubbles are evident in the impurity layer on the TEM micrograph (**b**). STEM-HAADF micrograph **(c)** and STEM-EDS maps of Fe**,** Mo**,** and Pt show that the impurity layer is Fe and Mo rich.

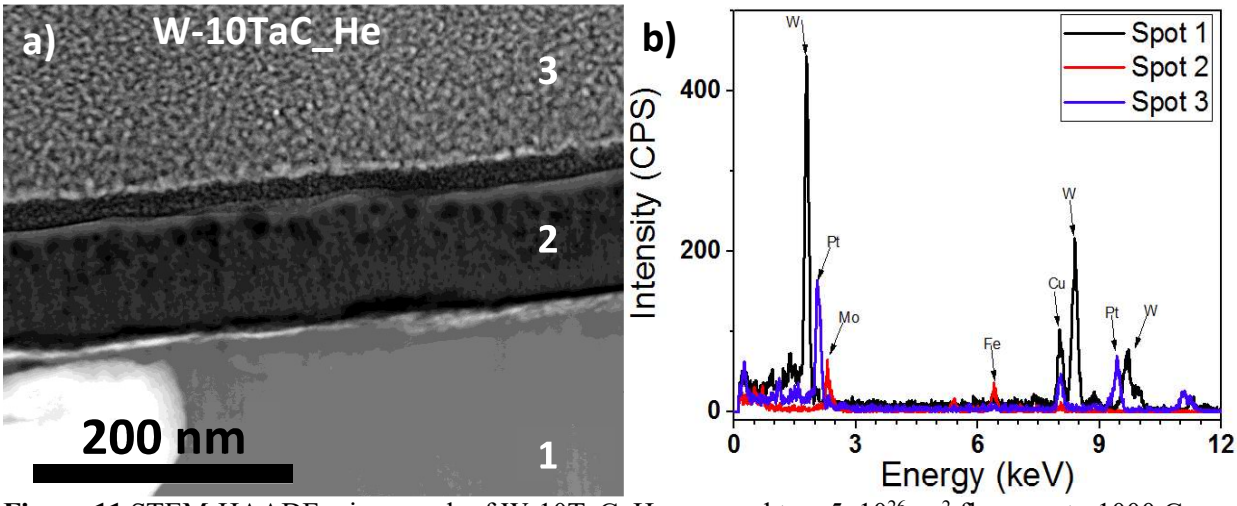

Figure 11 STEM-HAADF micrograph of W-10TaC_He exposed to a $5x10^{26}$ m^{-2} fluence at ~1000 C specimen showing ~80 nm thick impurity layer deposited on surface of sample. Helium bubbles are evident within the impurity layer, with an average size of 2.9±1.4 nm. EDS spectra collected at indicated points (1, 2, 3) are given in **(b)** confirming that Region 2 is an impurity layer rich in Mo and Fe.